

## RESEARCH ARTICLE

10.1029/2018JB016434

## Key Points:

- We incorporate von Karman regularization into geodetic Bayesian slip inversions to capture the fractal nature of slip
- We also solve for fault size using a transdimensional Bayesian inversion to remove bias caused by fault size in von Karman regularization
- Application to the 2016 Tottori, Japan, earthquake shows that contrary to some seismic studies, slip ruptured almost to the surface

## Supporting Information:

- Supporting Information S1
- Table S1
- Table S2
- Table S3
- Table S4
- Table S5
- Table S6

## Correspondence to:

R. M. J. Amey,  
R.M.J.Amey@leeds.ac.uk

## Citation:

Amey, R. M. J., Hooper, A., & Morishita, Y. (2019). Going to any lengths: Solving for fault size and fractal slip for the 2016,  $M_w$  6.2 Central Tottori earthquake, Japan, using a transdimensional inversion scheme. *Journal of Geophysical Research: Solid Earth*, 124, 4001–4016. <https://doi.org/10.1029/2018JB016434>

Received 24 JUL 2018

Accepted 8 MAR 2019

Accepted article online 14 MAR 2019

Published online 1 APR 2019

# Going to Any Lengths: Solving for Fault Size and Fractal Slip for the 2016, $M_w$ 6.2 Central Tottori Earthquake, Japan, Using a Transdimensional Inversion Scheme

R. M. J. Amey<sup>1</sup> , A. Hooper<sup>1</sup> , and Y. Morishita<sup>2</sup>

<sup>1</sup>COMET, School of Earth and Environment, University of Leeds, Leeds, UK, <sup>2</sup>Geospatial Information Authority of Japan, Tsukuba, Japan

**Abstract** Many earthquake properties, including slip, show self-similar (fractal) features. We can incorporate self-similarity into Bayesian slip inversions via von Karman correlation, so that the regularization applied is representative of observed fault features. In von Karman regularization, each slip patch has a relationship to every other patch. This means that von Karman regularization only has meaning when applied to patches that actually slipped; if applied to nonslipping patches, spurious slip can be added to meet the von Karman correlation criteria. Additionally, the fault size, usually chosen in advance, also affects the von Karman correlation lengths meaning that the final slip solution may be biased by initial geometry choices. Here we present a method for solving for the size of the fault plane during the slip inversion process, as well as slip, rake, and a hyperparameter controlling slip variance. We use a transdimensional Bayesian inversion scheme constrained by geodetic surface displacements and regularized using von Karman correlation. We use circular harmonics to solve for the size of the slipping area, to allow for a complex shape that is connected and continuous across the fault. We apply this method to the 2016  $M_w$  6.2 Central Tottori earthquake, Japan, constrained by interferometric synthetic aperture radar InSAR (Sentinel-1 and ALOS-2) and Global Navigation Satellite System data (GNSS). We find an area of slip extending from approximately 2- to 10-km depth, with the slipping area elongated in the downdip direction. In contrast to some seismic studies, we find slip ruptured most of the seismogenic layer.

## 1. Introduction

Assumptions incorporated into coseismic slip inversions should be realistic and justifiable for resulting slip distributions to be useful. Every prior assumption changes the final slip distribution, which is one of the reasons behind variability between slip results for the same earthquake (Minson et al., 2013). Most commonly used regularization techniques simply satisfy mathematical constraints (e.g., the Laplacian or minimum norm) and have no physical basis in how faults are seen to behave in nature.

There are several aspects of earthquakes that display fractal properties, which mathematically equates to a behavior following a power law function. Many recent papers suggest that earthquake slip also shows fractal properties. This includes measurements of surface coseismic slip (e.g., Milliner et al., 2015) analysis of published finite fault inversions (Mai & Beroza, 2002) and measurements of exhumed fault surface roughness (e.g., Candela et al., 2012). We therefore suggest that fractal slip properties should be incorporated into slip inversions, as this approach can better capture the physical properties of faults than other regularisation techniques (Amey et al., 2018).

Mai and Beroza's (2002) meta-analysis showed that the von Karman autocorrelation function best describes the long-order correlation of earthquake slip along a fault plane. Unlike a fractal correlation, which is only described by one variable (fractal dimension,  $D$ ), the von Karman correlation is controlled by the Hurst parameter,  $H$ , and additionally two correlation lengths. The Hurst parameter is related to the fractal dimension by  $D = (\text{Euclidian dimension} + 1 - H)$ , where a 2-D object has Euclidian dimension = 2. The von Karman correlation power decays more slowly at small wavenumbers and also captures the self-affine nature of slip through different correlation lengths in the along-strike and downdip directions.

We therefore regularize our inversions using von Karman correlation as a prior assumption. The von Karman autocorrelation function is given by

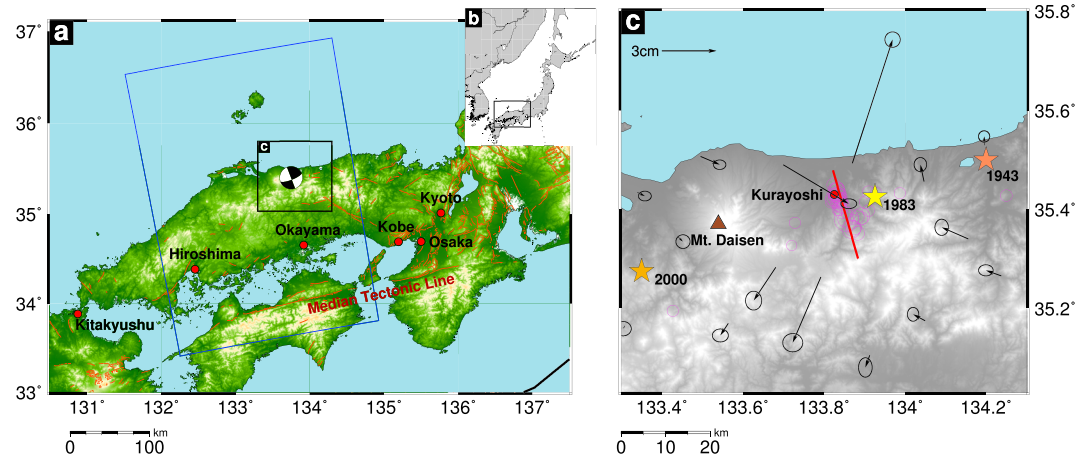


**Figure 1.** Regional setting of the Central Tottori earthquake. Insert (a) shows tectonic context of this earthquake (area of Japan shown in inset b). Onshore faults in the region shown in dark orange from the Research Group for Active Faults of Japan (1991), and the focal mechanism for the 2016  $M_w$  6.2 earthquake. Inset (c) shows aftershocks (open, magenta circles) and GNSS from the earthquake and past large earthquakes in the area (colored stars). Also shown is Mount Daisen (brown triangle) and the location of the city Kurayoshi (red circle). Our modeled fault is shown in red, based on InSAR and aftershock locations. One month of aftershocks from the National Research Institute for Earth Science and Disaster Resilience (2018) K-NET and KiK-net and GNSS from GNSS Earth Observation Network. GNSS = Global Navigation Satellite System.

$$\Sigma_s = \frac{G_H(r/a)}{G_H(0)} \quad (1)$$

where  $r$  is the distance between slip patches,  $a$  is the correlation length used to scale this distance,  $H$  is the Hurst parameter, and  $G_H(r/a) = (r/a)^H K_H(r/a)$  where  $K_H$  is a modified Bessel function of the second kind, of order  $H$  (Mai & Beroza, 2002).

We have developed a code, *slipBERI* (*slip* from *Bayesian Regularized Inversion*, with availability detailed in Acknowledgments section), to solve for slip in a Bayesian sense using von Karman regularization while simultaneously solving for rake and a hyperparameter that controls the degree of regularization.

But a complication with von Karman regularization is that it is dependent on the choice of fault size in two ways. First, the empirically derived along-strike and downdip correlation lengths,  $a_{as}$  and  $a_{dd}$ , which are used to calculate scaled distance  $r/a$ , depend on fault length and fault width respectively (Mai & Beroza, 2002). Second, in von Karman regularization each patch has a relationship with every patch. While this can provide a useful constraint for areas of the fault that are more poorly resolved than patches at the surface, it can result in patches that are almost in the model null space being assigned slip just to satisfy the von Karman regularization. This is particularly a problem at depth, where assigning slip may have little effect on the surface observations, and therefore little effect on the likelihood, but can increase the von Karman prior probability. Multiple patches with zero slip do not satisfy von Karman autocorrelation; if a chosen fault is larger than the area that slipped, then there should be zero slip around the edges, but this would lead to patches both near and far having 100% correlation, which the von Karman constraint prevents, and so a small amount of slip is placed there instead. This slip at depth is not representative of earthquake processes and instead is an artifact of the regularization. Consequently, the von Karman constraint introduces a bias in the inversion if applied to patches that are not slipping, both in assigning slip to patches where slip did not occur and also decreasing the maximum permitted magnitude elsewhere due to the correlation between all patches. There are methods that are used in slip inversions to avoid oversmoothing and instead produce a compact solution, including sparsity promoting methods (Evans & Meade, 2012). We cannot combine these methods with the von Karman regularization here, because due to the correlation between every patch, a sparse solution which contains some nonslipping patches would artificially decrease the slip value on other patches that are slipping.

Instead, in this study, in order to solve for slip using von Karman regularization but prevent oversmoothing, we present an algorithm for solving for the size of the slipping area within a Bayesian inversion. This method

enables us to remove any bias introduced by the choice of the size of the fault plane in advance of the inversion, thus limiting the dependence of the solution on subjective choices made prior to inversion.

We do this using a transdimensional MCMC (Markov chain Monte Carlo) approach (Green, 1995) that uses circular harmonics to control the shape, size, and orientation of the slipping area while ensuring that it is continuous. We apply this inversion technique to the  $M_w$  6.2 Central Tottori, Japan, earthquake (Figure 1). This occurred on 21 October 2016 and was a strike-slip earthquake with a small normal component. This example involves a fairly simple geometry, which allows us to test our new methodology on a simple, one-fault case study. However, we develop the theory for application to multistrand faults, to allow for application to more complicated fault geometries in the future. We use InSAR (interferometric synthetic aperture radar data) data acquired by Sentinel-1 and ALOS-2, and GNSS (Global Navigation Satellite System) data to constrain the surface displacements. Following the earthquake, ALOS-2 acquired extra acquisitions in a left-looking mode in addition to the normal right-looking acquisitions, for both ascending and descending orbits. These data combined with GNSS give high-resolution displacement measurements for this earthquake. During the inversion, we solve for the size of the fault plane as well as slip and rake of each patch, the reference displacement of every interferogram and a hyperparameter controlling the extent of smoothing. Finally, we present the slip results and comment on seismic hazard in this region.

This method we present provides a useful tool for analyzing continental earthquakes, removing any bias caused by fault size.

## 2. Methods

### 2.1. Model Setup

Initially, we choose a fault size with fixed strike and dip, using InSAR results and aftershock locations, and extend it along-strike and downdip to make it larger than the likely area that actually slipped. We break the fault plane down into equally sized rectangular patches and solve separately for slip magnitude and rake for each fault patch. We also solve for a hyperparameter,  $\alpha^2$ , which we discuss further in section 2.2.1.2, a constant offset for each of the InSAR scenes, equivalent to the displacement of the reference point, and circular harmonics terms, which are discussed below. Although we fix strike and dip in the inversions presented here, they can also be solved for as extra model parameters if necessary.

#### 2.1.1. Parameterizing Fault Size With Circular Harmonics

Having chosen in advance a fault plane that is expected to be too large, we then permit patches to turn “on” or “off” during the inversion. To ensure a continuous slipping area, we use circular harmonics, the 2-D version of spherical harmonics, to define the area; patches within this area are permitted to slip and those outside are considered to have zero slip. A patch is “on” if its center lies within the slipping area, and “off” otherwise. We use the first four terms of the circular harmonic expansions. For convenience, rather than solving for both positive and negative harmonics, we solve for the coefficient (size) and a rotation parameter,  $\phi$ , for each harmonic. We also solve for the  $x$  and  $y$  location of the center of slipping area relative to the top left of the fault (Figure 2).

We calculate the length and width of the slipping area defined by the harmonics, which feeds into equations used for calculating the von Karman probability, discussed in section 2.2.1.2.

We begin our inversion, described below, with the maximum permitted zero-order harmonic, such that the entire fault is on at the start of the inversion.

### 2.2. Bayesian Slip Inversion

We use a Bayesian approach as it allows us to incorporate prior assumptions on the model parameters, including the von Karman nature of slip. Also, the solution gives a suite of the models that fit the data within an acceptable level, allowing the quantification of the errors and trade-offs between model parameters (e.g., Benavente et al., 2019). It is also a flexible framework that allows us to easily incorporate features such as regularization, positivity constraints, and solving for the number of model parameters.

We have previously presented our method for solving for slip incorporating the von Karman regularization (Amey et al., 2018). Here we modify our scheme to allow for a variable number of slipping patches.

A Bayesian inversion aims to update the joint prior probability density function (PDF) for all the model parameters (unknowns) given the data. Our knowledge of what the model parameters should be before commencing the inversion is represented as a joint prior PDF for all of the model parameters. Throughout

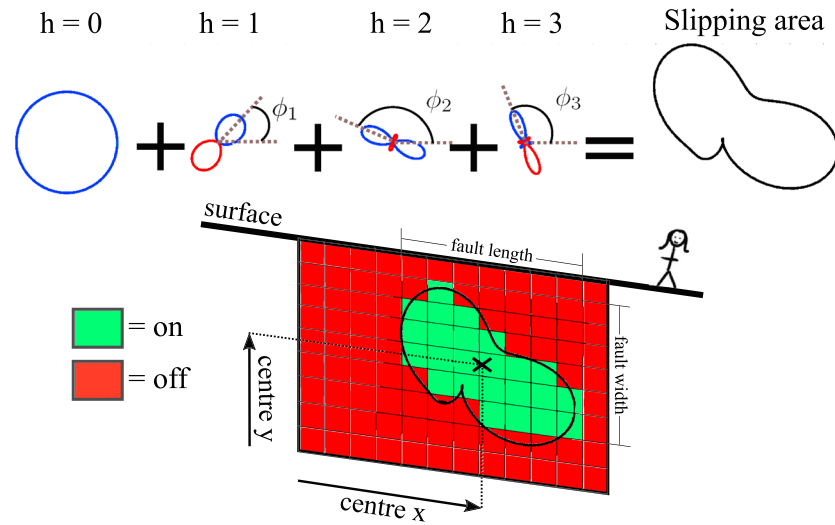


**Figure 2.** We use the first four terms of the circular harmonic expansion to define a slipping area on a fault plane. Patches within this slipping area are “on” and are permitted to slip, those outside are “off” and are considered to have zero slip. A patch is on if its center is within the slipping area. We solve for the coefficients (size) of each harmonic, as well as the rotation,  $\phi$ , and  $x, y$  location of the center of this slipping area on the fault plane.

the inversion, new trials are drawn for each parameter from their prior PDFs, then these prior PDFs are modified based on the likelihood (fit to data) to give the full posterior probability.

By Bayes' theorem extended to density functions, the posterior probability density,  $p(\mathbf{m}|\mathbf{d})$ , of a model,  $\mathbf{m}$ , given a set of data,  $\mathbf{d}$ , is given by

$$p(\mathbf{m}|\mathbf{d}) = \frac{p(\mathbf{d}|\mathbf{m})p(\mathbf{m})}{\int_{-\infty}^{\infty} p(\mathbf{d}|\mathbf{m})p(\mathbf{m})d\mathbf{m}} \quad (2)$$

where  $p(\mathbf{m})$  is the prior probability density of the model, which is the initial knowledge of the model parameters before commencing an inversion;  $p(\mathbf{d}|\mathbf{m})$  is the likelihood density function, which captures how well the data can be fit by a current model (the probability of  $\mathbf{d}$  given  $\mathbf{m}$ ). The denominator, sometimes called “evidence,” is a normalizing constant, as it is independent of the models (Sambridge et al., 2006).

Some posterior PDF solutions can be determined analytically, but we cannot do this here as we solve for slip, number of patches and additionally a hyperparameter,  $\alpha^2$ , representing the variance of slip within the inversion (discussed further in section 2.2.1.2). Instead, we must use some form of sampling to evaluate equation (2) for different models. For a large number of model parameters, sampling by means of a grid search quickly becomes impractical and so we use MCMC sampling. MCMC sampling is a way to efficiently sample a target distribution (Tarantola, 2005). It is a memoryless chain, in which during each iteration a new trial is generated by perturbing only the current state. We use the Metropolis-Hastings rule (Hastings, 1970; Metropolis et al., 1953), to decide whether to accept each trial; a new trial is accepted if it is more probable, but also less probable new trials are accepted if the ratio of the probabilities (named the acceptance ratio) is greater than a random number drawn between 0 and 1. This allows the chain to extract itself from local maxima. Thus, the chain moves and preferentially targets regions of parameter space with higher probabilities. Accepted trials are saved and new trials are drawn from the current model; rejected trials are discarded, and the previous state is saved. At the end of the inversion, the initial samples are also discarded as these are still influenced by the starting position and do not properly represent the posterior, but rather the “burn in.” The full posterior PDF is made up of all the saved trials.

The acceptance ratio,  $a$ , for a new trial  $m'$ , a perturbation of  $m$ , is given by

$$a(m'|m) = \min[1, \text{prior ratio} \times \text{likelihood ratio}] \quad (3)$$

$$a(m'|m) = \min[1, \frac{p(\mathbf{m}')}{p(\mathbf{m})} \times \frac{p(\mathbf{d}|\mathbf{m}')}{p(\mathbf{d}|\mathbf{m})}] \quad (4)$$

The acceptance ratio is compared to a random number between 0 and 1 in the Metropolis-Hastings rule. For a transdimensional case, extra terms must be considered in the acceptance ratio, which are frequently not included in the fixed dimensional case (as in equations (3) and (4)). The full acceptance ratio is

$$a(m'|m) = \min[1, \text{prior ratio} \times \text{likelihood ratio} \times \text{proposal ratio} \times \text{Jacobian}] \quad (5)$$

$$a(m'|m) = \min[1, \frac{p(\mathbf{m}')}{p(\mathbf{m})} \times \frac{p(\mathbf{d}|\mathbf{m}')}{p(\mathbf{d}|\mathbf{m})} \times \frac{q(\mathbf{m}|\mathbf{m}')}{q(\mathbf{m}'|\mathbf{m})} \times |J|] \quad (6)$$

where the proposal distribution is the distribution from which a new sample is drawn and the role of the Jacobian,  $J$ , is to account for scale changes between  $m$  and  $m'$  (Sambridge et al., 2006). For nontransdimensional inversions, the proposal distribution ratio and Jacobian are equal to 1, but this cannot be assumed for an inversion that changes dimension such as we use here.

In the following sections we describe each term in the acceptance ratio in turn and how they are calculated.

### 2.2.1. Prior

In our setup the prior can be broken down as the product of the independent prior for each model parameter, for example, the permitted range each model parameter can take, and the prior imposed by the von Karman constraint, used to ensure that the overall trials drawn represent a von Karman distribution.

#### 2.2.1.1. Model Parameter Priors

We define an independent prior probability distribution for each model parameter from which trials are drawn. We use boxcar priors for slip, rake, and InSAR offset, meaning that we assign a constant probability in a permitted range and zero probability outside of that range. While some studies put a prior on magnitude dip-slip and strike-slip motion, here our priors are on magnitude of slip and rake and these are the parameters for which we solve. Note that applying a uniform prior to dip slip and strike slip would result in a nonuniform prior on slip and rake, which is contrary to our assumption.

For the hyperparameter,  $\alpha^2$ , we use a logarithmic prior, discussed above, by solving for a model parameter  $\mathbf{q}$  with boxcar prior and setting  $\alpha^2$  by  $\alpha^2 = 10^{\mathbf{q}}$ . We notate  $\alpha^2$  in bold as it is a vector if solving for smoothing on different fault strands. For the circular harmonics parameters we also use boxcar priors and use the dimensions of the fault to set the maximum permitted values, such that the center  $x, y$  coordinates must be on the fault and any one harmonic cannot solely produce a slipping area larger than the fault.

The joint prior is the product of the independent priors for each parameter and includes a normalizing constant. Unlike in Amey et al. (2018), this constant cannot be ignored as it depends on the number of patches, which here changes throughout the inversion. For a transdimensional case, the prior can be expressed as follows:

$$p(\mathbf{m}) = p(\mathbf{m}|n)p(n) \quad (7)$$

where  $p(n)$  is the prior on the number of discrete slip patches,  $n$  (Bodin & Sambridge, 2009). We assume a constant prior probability for  $p(n)$  between 1 and the number of patches in our grid, and so  $p(n)$  can be ignored.

The slip and rake for the patch can be separated by

$$p(\mathbf{m}|n) = p(\mathbf{s}|n)p(\mathbf{r}|n) \quad (8)$$

where  $\mathbf{s}$  is slip and  $\mathbf{r}$  is rake. As discussed above we use a boxcar for both slip and rake. Thus, the prior probability of the patch slip given the number of slip patches is  $p(\mathbf{s}|n) = 1/(\Delta s)^n$  when all slips are within the permitted range and zero otherwise, where  $\Delta s$  is the range of permitted slip. The same is true for rake, that is,  $p(\mathbf{r}|n) = 1/(\Delta r)^n$ .

Thus, the transdimensional prior is

$$p(\mathbf{m}|n) = (\Delta \mathbf{s})^{-n} (\Delta \mathbf{r})^{-n} \quad (9)$$

For  $s$  and  $r$  within their prior ranges, and zero otherwise.

### 2.2.1.2. The von Karman Prior

As discussed above, fractal properties of slip are incorporated into the slip inversion using von Karman autocorrelation as a prior.

The von Karman prior probability of a trial slip solution is

$$p(\mathbf{s}) = (2\pi\alpha^2)^{-n/2} |\Sigma_s|^{-1/2} e^{-\frac{1}{2\alpha^2} \mathbf{s}^T \Sigma_s^{-1} \mathbf{s}} \quad (10)$$

where

- $p(\mathbf{s})$  = prior probability of this slip distribution;
- $\alpha^2$  = a hyperparameter controlling variance of slip;
- $n$  = number of slip patches currently on;
- $|\Sigma_s|$  = determinant of autocorrelation matrix;
- $\mathbf{s}$  = a vector of slip magnitude.

The correlation matrix calculation ( $\Sigma_s$ , calculated from equation (1)) is dependent on the Hurst parameter  $H$ , and the distance between fault patches, normalized by the correlation length. We find that when changing the size of the slipping area, the correlation matrix can become close to singular, so we add a stabilizing constant of 0.01 to the diagonal of  $\Sigma_s$ . The normalized distance,  $r/a$ , is calculated by scaling the along-strike and downdip distances between each fault patch by an along-strike,  $a_{as}$ , or downdip,  $a_{dd}$ , correlation length. We use the scaling relations from Mai and Beroza (2002) to calculate the correlation lengths:

$$a_{as} = 1860 + 0.34 \times (\text{fault length}) \text{ (meters)} \quad (11)$$

$$a_{dd} = -390 + 0.44 \times (\text{fault width}) \text{ (meters)} \quad (12)$$

These correlation lengths are dependent on length and width of the slipping area, which we recalculate as the size of the slipping area changes (section 2.1.1).

We use  $H_{dd} = 0.77$  and  $H_{as} = 0.71$  for downdip and along-strike Hurst parameters (Mai & Beroza, 2002).

The hyperparameter,  $\alpha^2$ , represents the variance of the slip distribution on each separately smoothed fault strand; the correlation matrix  $\Sigma_s$  defines the von Karman correlation and the hyperparameter  $\alpha^2$  scales this to produce the appropriate magnitude of slip.

Since we solve for the number of slip patches that are on within the inversion, the scalar  $n$  also changes as the slipping area is updated.

### 2.2.2. Likelihood

On the assumption that the errors are multivariate Gaussian, the likelihood is calculated by the fit of the current model to the observed data, weighted by the variance-covariance matrix and given by

$$p(\mathbf{d}|\mathbf{m}) = (2\pi)^{-N/2} |\Sigma_d|^{-1/2} e^{-\frac{1}{2} (\mathbf{d} - \mathbf{G}\mathbf{s} - \mathbf{k})^T \Sigma_d^{-1} (\mathbf{d} - \mathbf{G}\mathbf{s} - \mathbf{k})} \quad (13)$$

where

- $p(\mathbf{d}|\mathbf{m})$  = the probability of the observation for the current model;
- $N$  = total number of data points;
- $\Sigma_d$  = variance-covariance matrix of the data;
- $\mathbf{d}$  = vector of data (InSAR line of sight; GNSS, east, north, or up);
- $\mathbf{s}$  = vector of magnitude of slip;
- $\mathbf{G}$  = kernel matrix, calculated for the correct rake values;
- $\mathbf{k}$  = a vector of constants for InSAR data and zero for GNSS.

We use Okada (1985) equations for an elastic dislocation in a half-space to calculate the kernel  $\mathbf{G}$  for unit slip in line of sight for InSAR and for east, north, or up for GNSS on each fault patch, for the appropriate rake and dip. The product of kernel  $\mathbf{G}$  and slip on each patch,  $\mathbf{s}$ , gives the surface displacements at each InSAR and GNSS measurement for that slip distribution. Before commencing the inversion, we calculate kernels with pure strike-slip and dip-slip motion and sum the contribution of these for the current rake values, as we are solving for rake, by

$$\mathbf{G} = \mathbf{G}_{ss} \times \cos(\mathbf{rake}) + \mathbf{G}_{ds} \times \sin(\mathbf{rake}) \quad (14)$$

where  $\cos(\mathbf{rake})$  and  $\sin(\mathbf{rake})$  are diagonal matrices.

The  $\mathbf{G}$  matrix is updated with the constant InSAR offsets by vector  $\mathbf{k}$  of the same dimension as  $\mathbf{d}$ , containing offsets  $k_1$  to  $k_5$  corresponding to the five InSAR scenes, so that offset is added or subtracted to the data for the appropriate InSAR scene.

### 2.2.3. Proposal Distribution

In this inversion our proposal distributions for each model parameter, which defines how each parameter is perturbed during the Markov Chain, is a boxcar distribution between  $\pm$  each parameter's "step size."

By allowing the number of slip patches to change, the problem becomes transdimensional; the number of unknowns is itself unknown. This requires an extension of the MCMC methods discussed above in which the algorithm alternates between updating the value of the model parameters (the current state) and the number of model parameters (jumping between state spaces), for example, the reversible-jump MCMC (Green, 1995). In our algorithm we alternate so that on odd iterations we update the values of the model parameters, and on even iterations we update the size of the slipping area (the number of model parameters).

In this case we must consider the potential asymmetry of the proposal distribution. For a problem in which the proposal distribution is symmetric the forward proposal distribution of a step of model  $m \rightarrow m'$  is the same as the reverse proposal distribution of model  $m' \rightarrow m$  and the ratio of the two proposal distributions is equal to 1 (Bodin & Sambridge, 2009). Symmetry cannot however be assumed for every problem, and here we assess whether our inversion setup is symmetrical or asymmetrical, to demonstrate that it is symmetrical and consequently many of the parameters are equal to 1 and can be neglected.

For a new model, the proposal ratio can be broken down into

$$\frac{q(\mathbf{m}|\mathbf{m}')}{q(\mathbf{m}'|\mathbf{m})} = \frac{q(\mathbf{s}|\mathbf{m}')}{q(\mathbf{s}'|\mathbf{m})} \times \frac{q(\mathbf{r}|\mathbf{m}')}{q(\mathbf{r}'|\mathbf{m})} \times \frac{(\alpha^2|\mathbf{m}')}{(\alpha^2|\mathbf{m})} \times \frac{(\mathbf{k}|\mathbf{m}')}{(\mathbf{k}'|\mathbf{m})} \times \frac{q(\mathbf{h}|\mathbf{m}')}{q(\mathbf{h}'|\mathbf{m})} \quad (15)$$

where  $\mathbf{s}$  is the slip on the new/removed patch and  $\mathbf{r}$  is rake on all patches,  $\alpha^2$  is a hyperparameter,  $\mathbf{k}$  is the constant InSAR offset, and  $\mathbf{h}$  are the harmonic parameters that we use to define the slipping area. The parameter  $\mathbf{k}$  is in bold in this equation as it is a vector if solving for a different InSAR offset for multiple InSAR scenes.

Even though changes to the harmonic parameters can lead to the addition or deletion of patches, the number of harmonic parameters itself does not change and therefore  $q(\mathbf{h}|\mathbf{m}') = q(\mathbf{h}|\mathbf{m})$ , and the same reasoning can be used for  $\alpha^2$  and  $\mathbf{k}$ .

On addition of a new slip patch, we do not select a new magnitude of slip using a probability distribution, but instead, the new patch takes a constant value: its value before being turned off. If we were drawing a new magnitude from a distribution, then this probability must be included in the proposal distribution. But because the new patch reassumes the value it held before it was turned off, the probability of it having value is 1. The probability for a patch reassuming a constant value is thus a delta function, with the probability of its previous value equal to 1 and for all other values equal to 0, meaning that  $q(\mathbf{s}'|\mathbf{m}) = 1$ . When this slip patch is removed, the probability of removing the slip magnitude of this patch is  $q(\mathbf{s}|\mathbf{m}') = 1$ . Thus,  $q(\mathbf{s}'|\mathbf{m}) = q(\mathbf{s}|\mathbf{m}')$  for the addition of a patch, and likewise for the deletion of a patch. Thus, the proposal ratio for slip is always 1, and the same argument can be made for rake. Note that this would not be the case if the slip and rake values for a new patch were selected from a probability distribution, see Bodin and Sambridge (2009). The Jacobian, whose role is to account for scale changes between  $m$  and  $m'$  (Sambridge et al., 2006), is equal to 1 as the bijective transformation  $m \rightarrow m'$  involves only constants. In other words, there is a one-to-one correspondence between the elements in  $m$  and in  $m'$  and so no scaling is required.

This means that for our formulation of the transdimensional Bayesian method  $q(\mathbf{m}|\mathbf{m}') = q(\mathbf{m}'|\mathbf{m})$ , and thus, the proposal ratio is equal to 1 and can be ignored. This is essentially because by choosing on and off patches through circular harmonics the addition of a patch in  $m \rightarrow m'$  has the same probability as removal of that patch in  $m \rightarrow m'$ . Indeed, the circular harmonics setup can cause multiple patches to turn on and off during one iteration. The proposal ratio would not be equal to 1 if we had set up the problem to randomly choose a patch to delete or turn on, as then the probability of a patch being chosen would depend upon how many patches are on or off at that time. We note that in the special case of all patches being on at the start of the inversion, this does not hold. However, this phase of sampling is removed in the burn-in. We find that the inversion at no point turns all patches to off, the other end-member.

#### 2.2.4. Acceptance Ratio

As in Amey et al. (2018) we break the algorithm down into two separate Metropolis steps, to first draw a trial that is representative of the prior before calculating the likelihood (Tarantola, 2005, chap. 2, p. 52). The first Metropolis step considers only the prior ratio, in order to draw a von Karman trial, which is nontrivial to directly sample. Then the likelihood is only calculated for trials that pass this prior test, to avoid the unnecessary calculation if a prior probability is low.

At the start of an iteration each model parameter is perturbed from its current state such that a step is taken in parameter space. We generate samples from the individual model priors' directly: boxcar or logarithmic, as discussed above. For a boxcar prior PDF, random numbers are drawn and any that are outside of the permitted range are "bounced back" into the permitted bounds: if a trial is drawn that is outside of its permitted upper bounds  $X$  by  $x$  m (in the example of slip) we move the trial back into permitted bounds by  $\text{trial} = X - x$ . We show that the "bouncing back" approach still produces a symmetrical proposal distribution in the supplementary materials (Text S1 in the supporting information).

Once trials have been drawn from each model parameters' prior distribution, we use a prior acceptance ratio to draw a representative transdimensional and von Karman trial. This means that the first step is to apply the Metropolis-Hastings rule to the prior acceptance ratio,  $a_p$ :

$$a_p(m'|m) = \min[1, \text{prior ratio}] \quad (16)$$

$$a_p(m'|m) = \min \left[ 1, \frac{\Delta \mathbf{s}^{-n'} \Delta \mathbf{r}^{-n'} \times (2\pi \boldsymbol{\alpha}^2)^{-n'/2} |\Sigma'_s|^{-1/2} e^{-\frac{1}{2} \mathbf{s}'^T \Sigma_s^{-1} \mathbf{s}'}}{\Delta \mathbf{s}^{-n} \Delta \mathbf{r}^{-n} \times (2\pi \boldsymbol{\alpha}^2)^{-n/2} |\Sigma_s|^{-1/2} e^{-\frac{1}{2} \mathbf{s}^T \Sigma_s^{-1} \mathbf{s}}} \right] \quad (17)$$

where, as above, the proposal distribution is not included as it is assumed to be symmetric.

If a trial is accepted as a representative sample of the prior, the Metropolis-Hastings rule is applied for the second time to the likelihood acceptance ratio,  $a_l$ :

$$a_l(m'|m) = \min[1, \text{likelihood ratio}] \quad (18)$$

$$a_l(m'|m) = \min \left[ 1, \frac{(2\pi)^{-N/2} |\Sigma_d|^{-1/2} e^{-\frac{1}{2} (\mathbf{d} - \mathbf{G}' \mathbf{s}')^T \Sigma_d^{-1} (\mathbf{d} - \mathbf{G}' \mathbf{s}')}}{(2\pi)^{-N/2} |\Sigma_d|^{-1/2} e^{-\frac{1}{2} (\mathbf{d} - \mathbf{G} \mathbf{s})^T \Sigma_d^{-1} (\mathbf{d} - \mathbf{G} \mathbf{s})}} \right] \quad (19)$$

If accepted the trial model becomes a representative sample of the posterior distribution. If either of the two Metropolis rule applications lead to rejection, the previous saved model becomes the new representative sample.

### 3. Sensitivity Tests

We perform sensitivity tests during the first 10,000 iterations, to tune the proposal distribution for each model parameter. These sensitivity tests increase or decrease the step sizes of each model parameter depending on the rejection ratio (see ; Amey et al., 2018), aiming to meet an ideal rejection ratio (Roberts et al., 1997). After 10,000 iterations the step sizes are fixed, and these initial iterations are removed with the burn-in.

### 4. Synthetic Tests

We created a synthetic test to verify that our method is able to locate localized slip within a larger fault plane.

The test consists of a single plane, pure strike-slip fault, with one area of slip surrounded by patches of zero slip. The moment, length scale, and slip are consistent with a magnitude  $\sim 6$  earthquake (Wells & Coppersmith, 1994). The plane is broken into 160 1-km  $\times$  1-km patches. The slipping area has slip that is consistent with von Karman correlation, which we produced by transforming noisy slip into correctly spatially correlated slip (Lohman & Simons, 2005). We created synthetic measurements by calculating surface displacements expected for this slip distribution using Okada (1985) equations. We then used these surface displacements to invert for slip on a fault with the correct geometry.

We created a synthetic GNSS and InSAR data set and added spatially correlated noise to the InSAR data with a sill, nugget, and range of  $10^{-5}$  m<sup>2</sup>,  $10^{-6}$  m<sup>2</sup>, and 15 km respectively. We used InSAR measurements spaced

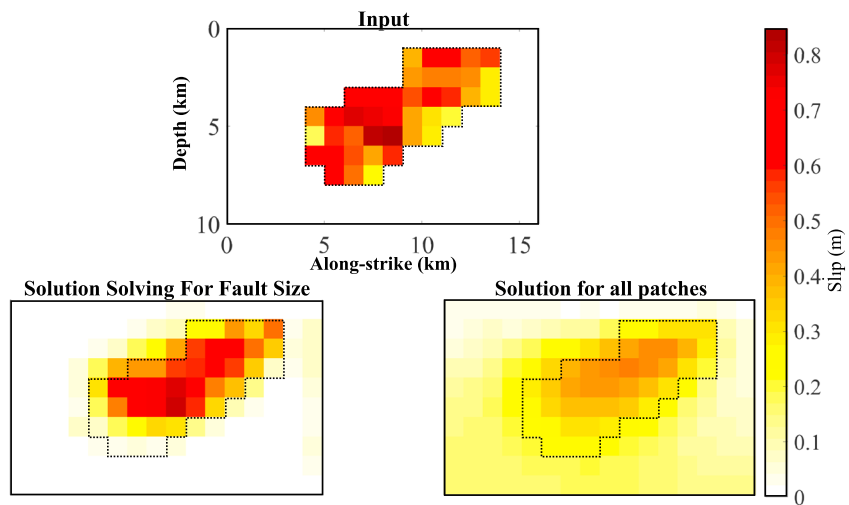


**Figure 3.** Synthetic test of transdimensional fault size inversion. Top figure shows the simulated true slip, with a slipping area consistent with von Karman slip surrounded by patches of zero slip. Bottom left shows the mean solution solving for slip and the size of the fault plane with von Karman regularization. Bottom right shows the inversion performed using von Karman regularization on all of the patches, for contrast. It is clear that the solution solving for fault size results in less smearing, since it is more likely to put zero slip in areas where the data do not require it.

every 400 m within 5 km of the fault and spaced every 2 km within 20 km of the fault. We randomly removed 800 InSAR data points (34%) to simulate loss of coherence. We scattered 40 GNSS data points within 20 km of the fault.

We solved for this input using our transdimensional inversion scheme detailed in section 2. We used a boxcar prior between 0 and 10 m for slip and a boxcar prior between  $150^\circ$  and  $210^\circ$  for rake. We used a logarithmic prior for  $\alpha^2$ , with a minimum permitted value of  $1 \times 10^{-4} \text{ m}^2$  and a maximum permitted value of  $10^{-2} \text{ m}^2$ . For the circular harmonic coefficients we used a boxcar between 0 and 15,000, for the circular harmonics center coordinates we used a boxcar between 0 and 15,000 m for  $x$ , and 0 and 20,559 m for  $y$  and for the circular harmonics rotation we use a boxcar between 0 and 100 radians, which is set arbitrarily high.

The results show that the transdimensional method is able to resolve the location of slip very well and also does a reasonable job of resolving magnitude (Figure 3). We plot the mean solution of the Bayesian inversion, that is, the mean of all saved values for each model parameter. If a patch is off during a saved iteration, we set the value to 0 for that iteration. Using mean slip of 0.1 m as a threshold, the method correctly identifies 37 patches out of 41 patches and misidentifies eight patches that are not slipping. At a 0.2-m threshold, the transdimensional approach puts slip on three patches that are not slipping. Also shown in Figure 3 is von Karman regularization performed on all patches, which results in smearing of slip over nearly all patches, with mean slip greater than 0.1 m on 82 nonslipping patches; at 0.2-m threshold it puts slip on 13 patches that are not slipping. The latter solution also does not correctly capture the magnitude of slip. The true moment of the synthetic test is  $6.95 \times 10^{17} \text{ Nm}$  (equivalent to a magnitude 5.9) earthquake and the transdimensional approach finds a very similar moment of  $6.79 \times 10^{17} \text{ Nm}$  (equivalent to a magnitude 5.9). The solution for all patches overestimates the moment, with a moment of  $9.64 \times 10^{17} \text{ Nm}$ , equivalent to a magnitude 6.0 earthquake. The fit to the data for both solutions is shown in supporting information Figures S1 and S2.

This synthetic example demonstrates the main advantages of our transdimensional method. Figure 3 shows that the inversion is able to resolve the location and magnitude of slip. This new method not only correctly identifies patches that did not slip in the earthquake as having zero slip but additionally better estimates the peak slip. This is because the peak slip value is not dragged down by its correlation with many surrounding patches with low slip.

## 5. Application to the Central Tottori Earthquake

### 5.1. Background

The earthquake occurred on 21 October 2016 in the Tottori prefecture of the Chugoku region of Japan, on Honshu island (Figure 1). Estimates of magnitude range from 6.2 (<https://earthquake.usgs.gov/>)

**Table 1**  
Permitted Bounds for the Boxcar Prior PDFs Used in This Inversion

	Min	Max
Slip (m)	0	10
Rake (degrees)	−40	20
InSAR offset (m)	−1	1
$\alpha^2$ (m <sup>2</sup> )	$1 \times 10^{-5}$	20
Circular harmonic coefficient	0	15,000
Along-strike circular harmonic center (m)	0	20,559
Down-dip circular harmonic center (m)	0	15,000
Circular harmonic rotation (radians)	0	$2\pi$

*Note.* The probability for each model parameter is 1 between these bounds, and 0 otherwise. PDF = probability density function; InSAR = interferometric synthetic aperture radar.

earthquakes/eventpage/us20007fta) and 6.6 from the Japan Meteorological Agency (Earthquake Research Committee, 2016) but fortunately caused no loss of life, though 30 people were injured and more than 300 houses were completely or partially destroyed (Kubo et al., 2017). It was a left-lateral strike-slip event on a roughly N-S striking fault plane, along which the aftershocks are distributed, 6 km south of the city of Kurayoshi. Peak ground velocities varied between 0.3 and 1.4 G, and the ground motion was widely felt over Southwest Japan (Kagawa et al., 2017).

This earthquake occurred in the Northern Chugoku shear zone, in the area geodetically identified and named San-in shear zone by Nishimura and Takada (2017). This shear zone has previously experienced large earthquakes, with a M 7.2 in 1943 (Kanamori, 1972), M 6.2 in 1983 (Tsukuda, 1988), and  $M_w$  6.6 in 2000 (Monelli et al., 2009; Semmane et al., 2005).

## 5.2. InSAR

We used Sentinel-1 (C-band SAR satellite) Ascending, Track 083, which had a 24-day repeat at this time. We processed Sentinel-1 data using the LiCSAR processing chain (Gonzalez et al., 2016). The SAR images for master (20161012) and slave (20161105) were downloaded from ESA's (European Space Agency) Copernicus Open Access Hub. Within LiCSAR the images were coregistered, multilooked twice in azimuth and 10 times in range, filtered, unwrapped, and geocoded. We found that the descending track was too decorrelated for the earthquake to be identified, which we put down to the large amount of vegetation and larger perpendicular baseline than the ascending track (82.1 m compared to 30.8 m).

We also used L-band ALOS-2 data; ultrafine-mode SAR data (spatial resolution of 3 m) from four different viewing directions (i.e., a combination of ascending/descending and right/left looking) were acquired by ALOS-2 within 5 days of the earthquake. A 10-m mesh Digital Elevation Model (Geospatial Information Authority of Japan, 2014) was used to remove the effect of topography. We applied tropospheric noise reduction using a numerical weather model provided by Japan Meteorological Agency (Kobayashi et al., 2014). To reduce long wavelength sources (i.e., caused by orbital errors, residual tropospheric delay, and ionospheric delay), InSAR displacements were fitted to the GNSS displacements using spline interpolation (Fukushima, 2013; Morishita, 2016).

We used a nested uniform downsampling approach to downsample the data for modeling. The region within approximately 25 km of the epicenter was downsampled 800 times, and outside this region was downsampled 2,500 times.

### 5.2.1. Variance-Covariance Matrix

Due to atmospheric changes between satellite acquisitions that are correlated in space, we calculated a variance-covariance matrix,  $\Sigma_d$  for each InSAR scene. We did this using the semivariogram method, details given in Amey et al. (2018).

## 5.3. Model set up

We fixed the fault geometry as given in supporting information Table S1 (see Figures 4 and 6 for geometry). We used 140 patches of approximately 1 km  $\times$  1 km (giving fewer model parameters than in the synthetic tests discussed above). The priors used in this study are given in Table 1. The proposal distribution for each model parameter is a uniform distribution between  $\pm$  each parameter's step size.

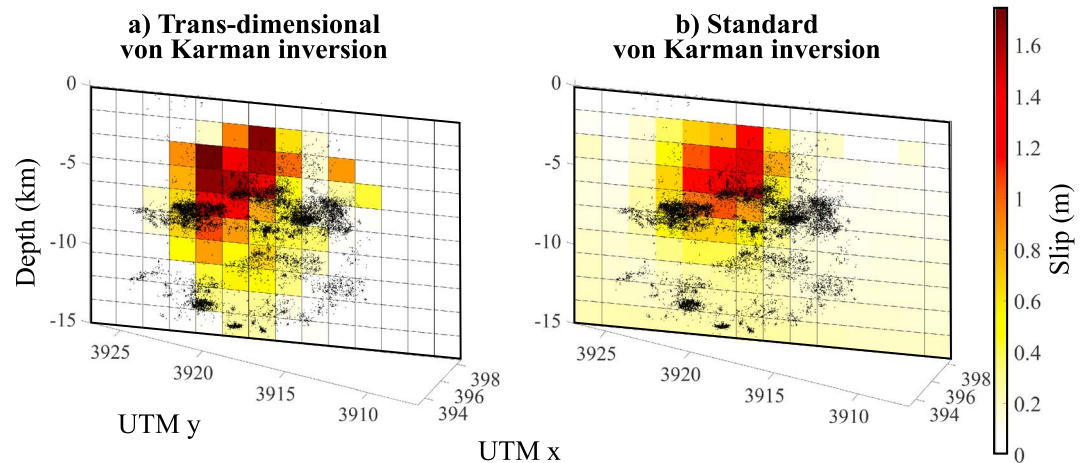


**Figure 4.** Mean slip for every patch from a von Karman regularized inversion for the Central Tottori 2016 earthquake. Panel (a) shows results for a transdimensional inversion using circular harmonics. Panel (b) shows von Karman regularization applied to the whole fault, where smearing has occurred. Black circles show 10 days of aftershocks from Ross et al. (2018) projected onto fault plane.

#### 5.4. GNSS

We used the data from continuous GNSS stations of the GNSS Earth Observation Network operated by the Geospatial Information Authority of Japan (GSI; Nakagawa, 2009; Sagiya, 2004). The site of 960640 was selected as a reference station, which is located >100 km ENE from the epicenter, where the coseismic displacement can be ignored. The coseismic displacements were calculated as the difference in the averages of the daily solutions between 6–20 October and 22 October to 5 November 2016. We assigned data uncertainties by calculating the standard deviations of the daily solutions for each station for the aforementioned dates after removing the displacement from the earthquake.

The GNSS shows up to a maximum of 6.8-cm movement at the GNSS stations nearest to the fault and is consistent with left-lateral motion (Figure 1).

#### 5.5. Results

We chose fault dimensions to be longer and deeper than the area of slip for an earthquake of this magnitude and the length scale of deformation from the InSAR. We judge convergence using the form of the histograms, the probability, and the values of the parameters through the length of the inversion. Additionally, we calculate the 95% confidence of the moment throughout the inversion and check that it has reached a steady value (supporting information Figure S3).

The mean slip for each patch, including solving for fault size, is shown in Figure 4a. As with the synthetic test, we take the mean of all saved values for each model parameter assuming zero slip when a patch is off. From the spatial pattern of time spent on by each patch (Figure 5) and the slip distribution, the earthquake slipped significantly from depths of approximately 1.5 km down to depths of approximately 10 km. There is a large patch with maximum average of approximately 1.7-m slip that lies of slip at a depth of 7 km. We repeated the inversion without solving for fault size (Figure 4b). This shows that peak slip is lower, with 1.3 m at a depth of 6 km, but this solution is smeared out, with some slip occurring on all deeper patches. Including solving for fault size in the inversion focuses the slip, leader to a larger area of high slip, extending at least 3 km further downdip. We show the MAP solution fit to data in Figures 6 and 7 to demonstrate the best fitting solution found. This solution fits the data well as does the solution applied to all patches, shown in supporting information Figures S4 and S5.

We compare the moment of these models to see if the smearing of a standard von Karman inversion is artificially inflating the moment. The 95% confidence interval of the moment for solving for slipping area is  $2.13 \times 10^{18}$  to  $2.70 \times 10^{18}$  Nm, which is slightly lower than the U.S. Geological Survey moment of  $2.82 \times 10^{18}$  Nm. The 95% confidence interval for the von Karman MAP solution applied to all patches is higher, with a range of  $2.60 \times 10^{18}$  and  $2.92 \times 10^{18}$ .

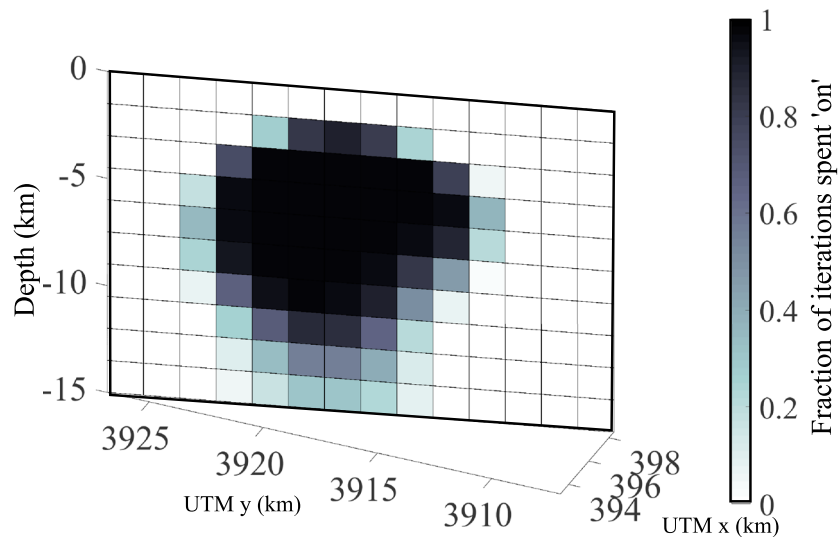


**Figure 5.** Fraction of time each patch is “on” during the inversion. This indicates that slip is required from the surface to around 12 km. Many other patches are “off” for nearly the entire inversion (the patch that is off the most is only turned on for 230 out of 2,000,000 iterations), indicating that slip there is not necessary to fit the data, and by the end of the burn-in these patches have been assigned as off.

## 6. Discussion

### 6.1. Implications for Seismic Hazard

The tectonics in Southwest Japan is dominated by the Philippine Sea plate subducting below the Eurasian plate at the Nankai trough. Two hundred kilometers north of the Nankai trough, the Median Tectonic line is a mature shear zone (Ross et al., 2018) as is evident from the topography and orientation of faults (Figure 1). But at 350 km north of the Nankai trough, the San-in Shear Zone (Nishimura & Takada, 2017; within the right-lateral Northern Chugoku shear zone ; Gutscher and Lallemand, 1999) in which these earthquakes occurred is less developed, without visible surface expressions of active faulting. But there have been several large earthquakes within this zone (Wesnousky et al., 1982), including, in the last century, a M 7.0 in 1943, a M 6.7 in 1943, and a  $M_w$  6.7 in 2000. This region has been geodetically identified as a right-lateral shear zone, but without a main fault along the axis of deformation, and with many conjugate Riedel shears orientated NW-SE left-lateral strike-slip faults instead (Nishimura & Takada, 2017), as observed in the 2016 earthquake and the 2000 western Tottori earthquake.

The 2000 and 2016 earthquakes occurred within approximately 30 km of the volcano Mount Daisen (Figure 1). In this area Zhao et al. (2018) observe significant crustal heterogeneity using seismic tomography, with a low-velocity anomaly, that they suggest is linked to fluid and arc magma, related to Mount Daisen. Additionally, they suggest that the subducting Philippine Sea plate is thinner under the Tottori region, leading to higher temperatures and increased slab dehydration reactions, causing hot upwelling in the Tottori region, which may have been the cause of the volcanic activity.

The San-in Shear zone fault zone is immature, as are the faults, which may be the reason for the unusually spatially extensive off-fault aftershock triggering (Ross et al., 2018). The aftershocks reveal geometric complexity at shallow (<8 km) depths, with many parallel faults, which may explain why the Tottori mainshock was so dissipative (Ross et al., 2018).

The area around the city of Kurayoshi has experienced many earthquakes greater than  $M_w$  6.2 in the past 40 years, and due to the ongoing subduction and fluids in the crust, is likely to experience large earthquakes again. Our results show that slip occurred from very near to the surface to approximately 10-km depth, through most of the seismogenic zone. However, the along-strike extent of the slipping area is only ~5 km, with a relatively constricted slipping area (Figure 4). This suggests that the fault could host another earthquake in the near future, along strike from where slip occurred in this earthquake. We note, however,

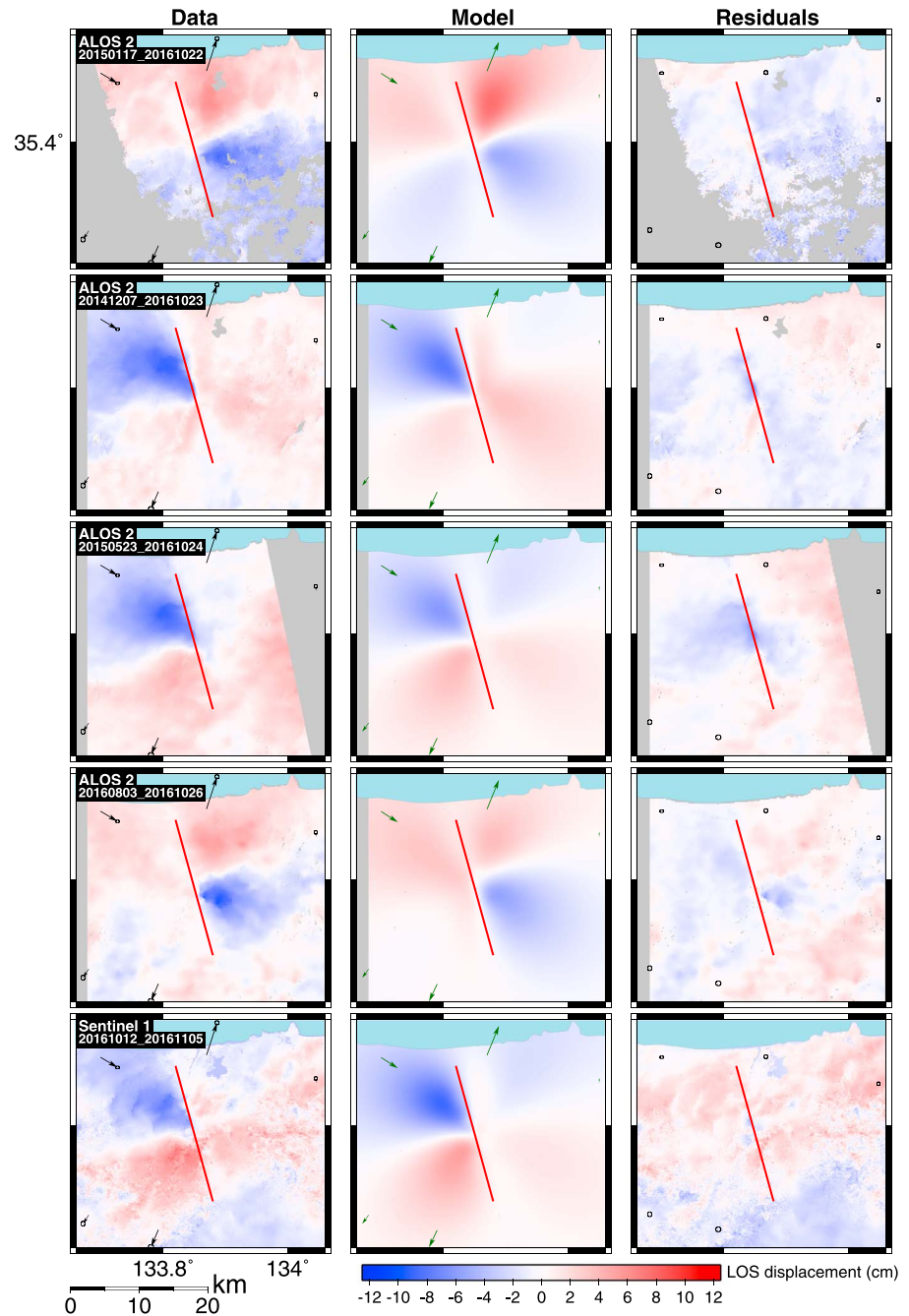


**Figure 6.** InSAR and near-field GNSS results for, from top, ALOS-2 ascending left looking, ALOS-2 descending left looking, ALOS-2 ascending right looking, ALOS-2 descending right looking, and Sentinel-1 ascending. The left-hand column shows the unwrapped interferograms, the middle column contains simulated interferograms for the MAP model, and the right-hand column displays residuals between the two. Positive is movement toward the satellite (e.g., uplift). The trace of all candidate fault patches is shown in red. GNSS vectors are shown in black, with 95% confidence intervals. Note that the residual GNSS vectors are too small to be easily seen, see Figure 7. GNSS = Global Navigation Satellite System; LOS = line of sight.

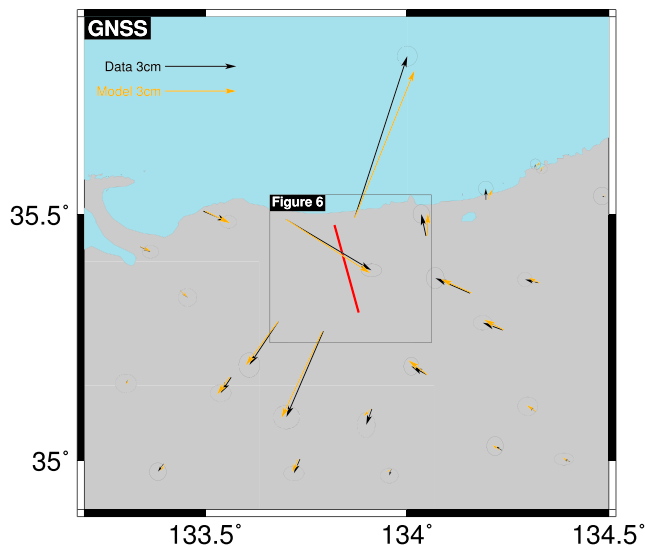


**Figure 7.** Global Navigation Satellite System (GNSS) displacements from 6 to 22 October 2016 for the 2016 Central Tottori earthquake, which occurred on 21 October 2016. Black arrows show the observed displacements, and orange arrows show the fit of the MAP model to the data. The fault trace is shown in red. Ellipses represent the 95% confidence intervals on the data.

that this modeling is a simplification, as we assume that all slip occurred on one fault plane, whereas the aftershocks indicate that there to be many subparallel fault structures at shallow depths (Ross et al., 2018).

### 6.2. Comparison to Published Results

We find the earthquake to have ruptured significantly from depths  $\sim 1.5$  km beneath the surface down to 10 km, suggesting that most of the seismogenic zone ruptured in this event. This is a similar result to the recently accepted geodetic study by Meneses-Gutierrez et al. (2019) and is in contrast to the seismological study by Ross et al. (2018), which suggests that significant slip occurred only at depths of  $\sim 10$ – $12$  km (supporting information Figure S6). Ross et al. (2018) find a concentrated slip patch of  $\sim 5$ -m slip with 93% of the seismic moment released below 8 km, which would leave the surface at risk from further faulting and considerable seismic hazard. Ross et al. (2018) also estimate a much higher peak slip (maximum of 5 m of slip), whereas we estimate a peak slip of 1.8 m. Kubo et al. (2017), however, find two distinct slipping patches of 0.6-m slip from 3-km depth down to 12-km depth, supporting our view that most of the seismogenic zone ruptured, though the peak slip magnitude is only 0.6 m. The InSAR data also encompass several days to weeks of activity after the earthquake (up to 4 days for the four ALOS-2 scenes and 15 days for Sentinel-1), which means there could be postseismic and aftershock signal included in our data. All of the InSAR scenes include the 70 foreshocks in the preceding 12 hr, but the largest foreshock, with magnitude  $M_w$  4.2 (Ross et al., 2018), represents only  $5 \times 10^{15}$  Nm of moment, which is less than 1% of the moment of the  $M_w$  6.2 event.

### 6.3. Convergence

Due to the quantized nature of turning patches on and off, the histograms of slip on each patch are not all as smooth as we would usually expect to determine convergence. Patches that are off for most iterations are

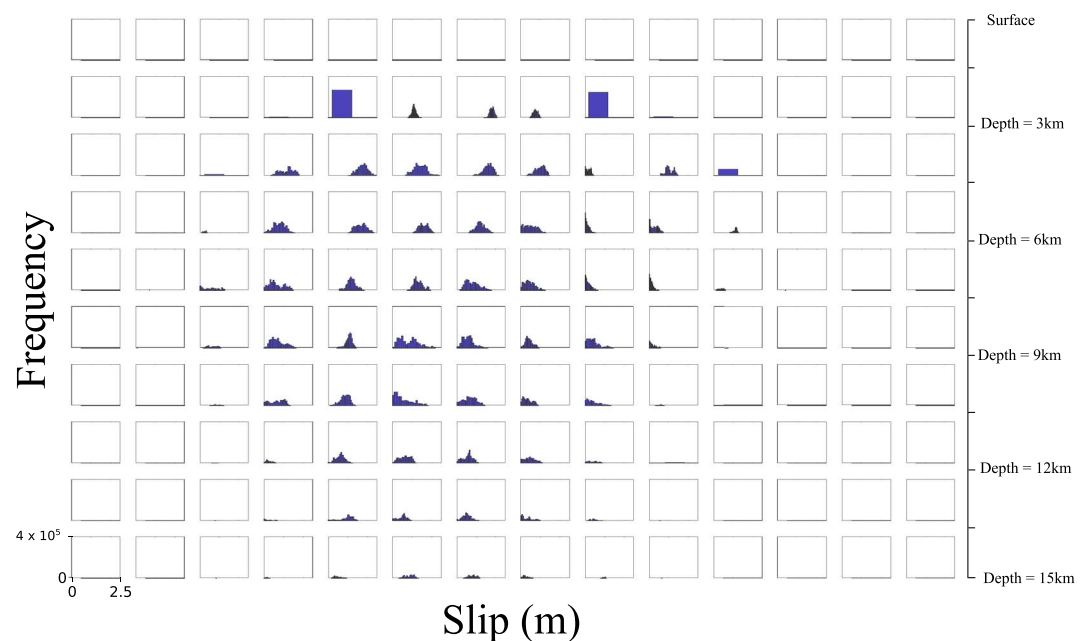


**Figure 8.** Histograms of sampled slip for every fault patch. Every histogram is plotted on the same scale, shown on the bottom left figure, and the histograms are plotted such that each histogram correlates with the patch's position on the fault plane. The patches that are “on” for the majority of the inversion have smoother, well-filled out histograms, suggesting this inversion has converged. Those that are only on for a small percentage of the time (see Figure 5, e.g., the bottom three rows) have fewer samples and are therefore less smooth.

sampled less, leading to rougher histograms (e.g., see bottom rows of Figure 8, corresponding to slip patches at the bottom of the fault). Therefore, we judge convergence based on the histograms for patches that were on for the majority of the inversion only.

#### 6.4. Expansion of Work

In this work we have used rectangular patches and have only permitted patches to turn on in predetermined positions. However, the inversion scheme is completely flexible; Dettmer et al. (2014), for example, used Voronoi cells in a seismological slip inversion. This approach could be incorporated into our inversion scheme, to determine the size of the patches based on resolution during the inversion, as has been done previously in advance of the inversion (Atzori & Antonioli, 2011; Barnhart & Lohman, 2010). We note, however, that the transdimensional approach can lead to instabilities in the inverse of the von Karman autocorrelation matrix,  $\Sigma_s$ , increasingly so for a larger number of slip patches. We minimize this by adding a small stabilizing constant to the diagonal of  $\Sigma_s$ ; however, more testing is required to determine if this approach can be used for any number of slipping patches.

### 7. Conclusions

In this study we present a new method for solving for the size of a slipping area within a von Karman regularized inversion. We suggest that von Karman regularization should be the default for slip inversions, since it captures the self-similar nature of slip, leading to tighter constraints on slip location. Solving for the size of the slipping area during the inversion removes any bias due to incorrectly choosing the fault length and width in advance. Application to the 2016 Central Tottori earthquake shows the earthquake ruptured from near the surface down to 10-km depth, representing a large portion of the entire seismogenic zone, in contrast to some seismological studies. This implies that an earthquake rupturing the up-dip part of the fault is unlikely in the near future. However, the along-strike extent of the slipping area was very tight, suggesting that the fault could host another along strike.

#### Acknowledgments

This work was supported by the National Environment Research Council (NERC) through the Leeds-York Doctoral Training Programme, grant NE/L002574/1. ALOS-2 data were provided under a cooperative research contract between GSI and JAXA. All Sentinel-1 data that were used are derived works of Copernicus data (2017) and are available to download through the ESA Copernicus Sentinel program. The downsampled InSAR and GNSS data are available in the supporting information. The code *slipBERI* is downloadable from <https://github.com/ruthamey/slipBERI>. We are grateful to Tom Ingleby for many useful discussions and Kaarsten Spaans for help with LiCSAR.

#### References

- Amey, R. M. J., Hooper, A., & Walters, R. J. (2018). A Bayesian method for incorporating self-similarity into earthquake slip inversions. *Journal of Geophysical Research: Solid Earth*, *123*, 6052–6071. <https://doi.org/10.1029/2017JB015316>
- Atzori, S., & Antonioli, A. (2011). Optimal fault resolution in geodetic inversion of coseismic data. *Geophysical Journal International*, *185*(1), 529–538. <https://doi.org/10.1111/j.1365-246X.2011.04955.x>
- Barnhart, W. D., & Lohman, R. B. (2010). Automated fault model discretization for inversions for coseismic slip distributions. *Journal of Geophysical Research*, *115*, B10419. <https://doi.org/10.1029/2010JB007545>
- Benavente, R., Dettmer, J., Sambridge, M., & Cummins, P. R. (2019). Efficient Bayesian uncertainty estimation in linear finite fault inversion with positivity constraints by employing a log-normal prior. *Geophysical Journal International*, *217*(1), 469–484. <https://doi.org/10.1093/gji/ggz044>
- Bodin, T., & Sambridge, M. (2009). Seismic tomography with the reversible jump algorithm. *Geophysical Journal International*, *178*(3), 1411–1436. <https://doi.org/10.1111/j.1365-246X.2009.04226.x>
- Candela, T., Renard, F., Klinger, Y., Mair, K., Schmittbuhl, J., & Brodsky, E. E. (2012). Roughness of fault surfaces over nine decades of length scales. *Journal of Geophysical Research*, *117*, B08409. <https://doi.org/10.1029/2011JB009041>
- Dettmer, J., Benavente, R., Cummins, P. R., & Sambridge, M. (2014). Trans-dimensional finite-fault inversion. *GJI Seismology*, *199*, 735–751. <https://doi.org/10.1093/gji/ggu280>
- Earthquake Research Committee (2016). Evaluation of earthquake in the Central Tottori Prefecture on October, 21, 2016. [http://www.jishin.go.jp/main/chousa/16nov\\_tottori/index-e.htm](http://www.jishin.go.jp/main/chousa/16nov_tottori/index-e.htm)
- Evans, E. L., & Meade, B. J. (2012). Geodetic imaging of coseismic slip and postseismic afterslip: Sparsity promoting methods applied to the Great Tohoku earthquake. *Geophysical Research Letters*, *39*, L11314. <https://doi.org/10.1029/2012GL051990>
- Fukushima, Y. (2013). Correction of DInSAR noise using GNSS measurements. In *APSAR2013*, pp. 226–228.
- Geospatial Information Authority of Japan (2014). Overview and types of digital elevation model of fundamental geospatial data.
- Gonzalez, P., Walters, R., Hutton, R., Spaans, K., McDougill, A., Hooper, A., & Wright, T. (2016). LiCSAR: Tools for automated generation of Sentinel-1 frame interferograms. in AGU Fall Meeting.
- Green, P. J. (1995). Reversible jump Markov chain Monte Carlo computation and Bayesian model determination. *Biometrika*, *82*(4), 711–732. <https://doi.org/10.1093/biomet/82.4.711>
- Gutscher, M.-A., & Lallemand, S. (1999). Birth of a major strike-slip fault in SW Japan. *Terra Nova*, *11*(5), 203–209. <https://doi.org/10.1046/j.1365-3121.1999.00247.x>
- Hastings, W. (1970). Monte Carlo sampling methods using Markov chains and their applications. *Biometrika*, *57*(1), 97–109. <https://doi.org/10.1093/biomet/57.1.97>
- Kagawa, T., Noguchi, T., Yoshida, S., & Yamamoto, S. (2017). Effect of the surface geology on strong ground motions due to the 2016 Central Tottori Earthquake, Japan. *Earth, Planets and Space*, *69*(1), 106. <https://doi.org/10.1186/s40623-017-0689-0>
- Kanamori, H. (1972). Determination of effective tectonic stress associated with earthquake faulting. The Tottori earthquake of 1943. *Physics of the Earth and Planetary Interiors*, *5*, 426–434. [https://doi.org/10.1016/0031-9201\(72\)90114-8](https://doi.org/10.1016/0031-9201(72)90114-8)
- Kobayashi, T., Ishimoto, M., Tobita, M., & Yurai, H. (2014). A tool for reduction of atmosphere-related noises included in an InSAR image, incorporating a numerical weather model. *J. GSI (in Japanese)*, *125*, 31–38.

- Kubo, H., Suzuki, W., Aoi, S., & Sekiguchi, H. (2017). Source rupture process of the 2016 central Tottori, Japan, earthquake (MJMA 6.6) inferred from strong motion waveforms. *Earth, Planets and Space*, 69, 10. <https://doi.org/10.1186/s40623-017-0714-3>
- Lohman, R. B., & Simons, M. (2005). Some thoughts on the use of InSAR data to constrain models of surface deformation: Noise structure and data downsampling. *Geochemistry, Geophysics, Geosystems*, 6, Q01007. <https://doi.org/10.1029/2004GC000841>
- Mai, P. M., & Beroza, G. C. (2002). A spatial random field model to characterize complexity in earthquake slip. *Journal of Geophysical Research*, 107(B11), 2308. <https://doi.org/10.1029/2001JB000588>
- Meneses-Gutierrez, A., Nishimura, T., & Hashimoto, M. (2019). Coseismic and postseismic deformation of the 2016 Central Tottori earthquake and its slip model. *Journal of Geophysical Research: Solid Earth*, 124. <https://doi.org/10.1029/2018JB016105>
- Metropolis, N., Rosenbluth, A. W., Rosenbluth, M. N., Teller, A. H., & Teller, E. (1953). Equation of state calculations by fast computing machines. *The Journal of Chemical Physics*, 21(6), 1087–1092. <https://doi.org/10.1063/1.1699114>
- Milliner, C. W., Dolan, J. F., Hollingsworth, J., Leprince, S., Ayoub, F., & Sammis, C. (2015). Quantifying near-field and off-fault deformation patterns of the 1992 Mw 7.3 Landers earthquake. *Geochemistry, Geophysics, Geosystems*, 16, 1525–2027. <https://doi.org/10.1002/2014GC005693>
- Minson, S. E., Simons, M., & Beck, J. L. (2013). Bayesian inversion for finite fault earthquake source models I—Theory and algorithm. *Geophysical Journal International*, 194(3), 1701–1726. <https://doi.org/10.1093/gji/ggt180>
- Monelli, D., Mai, P. M., Jónsson, S., & Giardini, D. (2009). Bayesian imaging of the 2000 Western Tottori (Japan) earthquake through fitting of strong motion and GPS data. *Geophysical Journal International*, 176(1), 135–170.
- Morishita, Y. (2016). Reduction of spatially long wavelength noises in SAR interferograms using GNSS data. *Journal of the Geodetic Society of Japan (In Japanese with English abstract)*, 62(2), 89–100. <https://doi.org/10.11366/sokuchi.62.89>
- National Research Institute for Earth Science and Disaster Resilience (2018). Strong-motion seismograph networks. <http://www.kyoshin.bosai.go.jp/>
- Nakagawa, H. (2009). Development and validation of GEONET new analysis strategy (Version 4). *Journal of Geographical Survey Institute (in Japanese)*, 118, 1–8.
- Nishimura, T., & Takada, Y. (2017). San-in shear zone in southwest Japan, revealed by GNSS observations. *Earth, Planets and Space*, 69(1), 85. <https://doi.org/10.1186/s40623-017-0673-8>
- Okada, Y. (1985). Surface deformation due to shear and tensile faults in a half-space. *Bulletin of the Seismological Society of America*, 75(4), 1135–1154.
- Research Group for Active Faults of Japan (1991). Active faults in Japan: Sheet maps and inventories. revised edition.
- Roberts, G. O., Gelman, A., & Gilks, W. R. (1997). Weak convergence and optimal scaling of random walk Metropolis algorithms. *The Annals of Applied Probability*, 7(1), 110–120. <https://doi.org/10.1214/aoap/1034625254>
- Ross, Z. E., Kanamori, H., Hauksson, E., & Aso, N. (2018). Dissipative intraplate faulting during the 2016 M w 6.2 Tottori, Japan earthquake. *Journal of Geophysical Research: Solid Earth*, 123, 1631–1642. <https://doi.org/10.1002/2017JB015077>
- Sagiya, T. (2004). A decade of GEONET: 1994–2003—The continuous GPS observation in Japan and its impact on earthquake studies. *Earth, Planets and Space*, 56(8), xxix–xli. <https://doi.org/10.1186/BF03353077>
- Sambridge, M., Gallagher, K., Jackson, A., & Rickwood, P. (2006). Trans-dimensional inverse problems, model comparison and the evidence. *Geophysical Journal International*, 167(2), 528–542. <https://doi.org/10.1111/j.1365-246X.2006.03155.x>
- Semmane, F., Cotton, F., & Campillo, M. (2005). The 2000 Tottori earthquake: A shallow earthquake with no surface rupture and slip properties controlled by depth. *Journal of Geophysical Research*, 110, B03306. <https://doi.org/10.1029/2004JB003194>
- Tarantola, A. (2005). *Inverse problem theory and methods for model parameter estimation* (pp. 50–52). Philadelphia: Society for Industrial and Applied Mathematics. <https://doi.org/10.1137/1.9780898717921.ch2>
- Tsukuda, T. (1988). Coda-Q before and after the 1983 Misasa earthquake of M 6.2, Tottori Prefecture, Japan. *Pure and Applied Geophysics PAGEOPH*, 128(1-2), 261–279. <https://doi.org/10.1007/BF01772600>
- Wells, D. L., & Coppersmith, K. J. (1994). New empirical relationships among magnitude, rupture length, rupture width, rupture area, and surface displacement. *Bulletin of the Seismological Society of America*, 84(4), 974–1002.
- Wesnousky, S. G., Scholz, C. H., & Shimazaki, K. (1982). Deformation of an island arc: Rates of moment release and crustal shortening in intraplate Japan determined from seismicity and Quaternary fault data. *Journal of Geophysical Research*, 87(B8), 6829–6852. <https://doi.org/10.1029/JB087iB08p06829>
- Zhao, D., Liu, X., & Hua, Y. (2018). Tottori earthquakes and Daisen volcano: Effects of fluids, slab melting and hot mantle upwelling. *Earth and Planetary Science Letters*, 485, 121–129. <https://doi.org/10.1016/J.EPSL.2017.12.040>